arXiv:1405.3847v1 [nucl-th] 15 May 2014

Relativistic equation of state at subnuclear densities in the Thomas-Fermi approximation

Z. W. Zhang and H. Shen

School of Physics, Nankai University, Tianjin 300071, China

shennankai@gmail.com

ABSTRACT

We study the non-uniform nuclear matter using the self-consistent Thomas–Fermi approximation with a relativistic mean-field model. The non-uniform matter is assumed to be composed of a lattice of heavy nuclei surrounded by dripped nucleons. At each temperature T, proton fraction Y_p, and baryon mass density ρ_B, we determine the thermodynamically favored state by minimizing the free energy with respect to the radius of the Wigner–Seitz cell, while the nucleon distribution in the cell can be determined self-consistently in the Thomas–Fermi approximation. A detailed comparison is made between the present results and previous calculations in the Thomas–Fermi approximation with a parameterized nucleon distribution that has been adopted in the widely used Shen EOS.

Subject headings: dense matter — equation of state — supernovae: general
Online-only material: color figures

1. Introduction

The equation of state (EOS) of hot and dense matter is an essential ingredient in understanding many astrophysical phenomena, e.g., supernova explosions and neutron star formations (Burrows et al. 2006; Janka et al. 2007; Sumiyoshi et al. 2005, 2009; Shen et al. 2011). The EOS for the core-collapse supernova simulations must cover wide ranges of temperature, proton fraction, and baryon density (see Table 1 of Shen et al. (2011)). Therefore, it is very difficult to build a complete EOS covering the wide range of thermodynamic conditions. Many efforts have been made to investigate the EOS of nuclear matter for the use of supernova simulations and neutron star calculations (Lattimer & Swesty 1991; Lattimer & Prakash 2007; Shen et al. 1998a,b, 2011; Schaffner & Mishustin 1996; Weber 2005). There are two commonly used EOSs in supernova simulations, namely the Lattimer–Swesty EOS (Lattimer & Swesty 1991), which employed a compressible liquid-drop model

with a Skyrme force, and the Shen EOS (Shen et al. 1998b, 2011), which used a relativistic mean-field (RMF) model and Thomas–Fermi approximation with a parameterized nucleon distribution. Recently, G. Shen et al. (2010) constructed the EOS based on a relativistic Hartree calculation for the Wigner–Seitz cell which includes nuclear shell effects. These EOSs employ the so-called single nucleus approximation (SNA), in which only a single representative nucleus is included instead of a distribution of different nuclei. It would be desirable to consider the mixture of nuclei based on nuclear statistical equilibrium (Hempel & Schaffner-Bielich 2010; Blinnikov et al. 2011; Furusawa et al. 2011, 2013). The mixture of nuclei is important for electron captures on nuclei inside supernova core. However, it has been demonstrated that SNA is a reasonable approximation for thermodynamical quantities (Burrows et al. 1984). In SNA, the thermodynamically favored nucleus is described by a compressible liquid-drop model in the Lattimer–Swesty EOS or by a Thomas–Fermi approximation with parameterized nucleon distribution in the Shen EOS. In this paper, we intend to study the matter at subnuclear densities, in which the heavy nucleus is described by a self-consistent Thomas–Fermi approximation.

The self-consistent Thomas–Fermi approximation has been widely used in atomic and nuclear physics. Many properties of nuclei can be described by the Thomas–Fermi approximation with good agreement to experimental data (Centelles et al. 2007). Recently, the self-consistent Thomas–Fermi approximation has been used to study nuclear pasta phases at subnuclear densities at zero temperature (Avancini et al. 2009) and finite temperature (Avancini et al. 2010), where the pasta phases include droplets (bubbles), rods (tubes), and slabs for three, two, and one dimensions, respectively. In our previous work (Shen et al. 1998a,b, 2011), a parameterized nucleon distribution was assumed in the Thomas–Fermi approximation and only droplet phase was taken into account. It is, however, not clear how good/bad the assumed nucleon distribution functions are in Shen EOS. Also, whether other pasta phases, like bubble phase, can make a meaningful difference in the transition to uniform nuclear matter. The main purpose of the present work is to study the non-uniform matter at subnuclear densities using the self-consistent Thomas–Fermi approximation. By comparing the nucleon distributions and thermodynamic quantities, we can examine the difference between the self-consistent Thomas–Fermi (STF) approximation and the parameterized Thomas–Fermi (PTF) approximation. In the present work, we consider both droplet and bubble configurations in order to investigate the effect of including the bubble phase, while other pasta phases are neglected for simplicity.

For the effective nuclear interaction, we use the relativistic mean-field (RMF) theory, in which nucleons interact via the exchange of isoscalar scalar and vector mesons (σ and ω) and an isovector vector meson (ρ). In this work, we employ the RMF theory including nonlinear σ and ω terms with the parameter set TM1 (Sugahara & Toki 1994). It is known

that the RMF theory with the parameter set TM1 can well reproduce ground state properties of finite nuclei including unstable ones (Sugahara & Toki 1994), and predicts a maximum neutron-star mass of 2.18 $M_\odot$ (Shen et al. 2011). In Shen EOS, the RMF results of TM1 were taken as input in the PTF calculation. Therefore, a detailed comparison can be made between the STF and PTF approximations based on the same RMF theory.

This paper is organized as follows. In Section 2, we briefly explain the RMF theory and the STF approximation for the non-uniform matter at subnuclear densities. In Section 3, we discuss the calculated results of the STF approximation in comparison with those obtained in the PTF approximation. Section 4 is devoted to the conclusions.

2. Formalism

We first give a brief description of the RMF theory (Serot & Walecka 1986; Sugahara & Toki 1994). We employ the RMF theory to calculate the properties of uniform matter. For non-uniform matter where nuclei exist to decrease the free energy, we use the STF approximation in which the RMF Lagrangian is used to derive the equations of motion for the fields (Avancini et al. 2009).

In the RMF theory, nucleons interact via the exchange of mesons. The exchanged mesons are isoscalar scalar and vector mesons (σ and ω) and isovector vector meson (ρ). We adopt the RMF theory with nonlinear σ and ω terms (Sugahara & Toki 1994). For a system consisting of protons, neutrons, and electrons, the Lagrangian density reads,

$$\begin{aligned}
\mathcal{L}_{\rm RMF} &= \sum_{i=p,n} \bar{\psi}_i \left[i\gamma_\mu \partial^\mu - M - g_\sigma \sigma - g_\omega \gamma_\mu \omega^\mu - g_\rho \gamma_\mu \tau_a \rho^{a\mu} - e\gamma_\mu \frac{1+\tau_3}{2} A^\mu \right] \psi_i \\
&\quad + \bar{\psi}_e \left[i\gamma_\mu \partial^\mu - m_e + e\gamma_\mu A^\mu \right] \psi_e \\
&\quad + \frac{1}{2}\partial_\mu \sigma \partial^\mu \sigma - \frac{1}{2} m_\sigma^2 \sigma^2 - \frac{1}{3} g_2 \sigma^3 - \frac{1}{4} g_3 \sigma^4 \\
&\quad - \frac{1}{4} W_{\mu\nu} W^{\mu\nu} + \frac{1}{2} m_\omega^2 \omega_\mu \omega^\mu + \frac{1}{4} c_3 \left(\omega_\mu \omega^\mu \right)^2 \\
&\quad - \frac{1}{4} R^a_{\mu\nu} R^{a\mu\nu} + \frac{1}{2} m_\rho^2 \rho^a_\mu \rho^{a\mu} - \frac{1}{4} F_{\mu\nu} F^{\mu\nu}, \qquad (1)
\end{aligned}$$

where $W^{\mu\nu}$, $R^{a\mu\nu}$, and $F^{\mu\nu}$ are the antisymmetric field tensors for ω^μ, $\rho^{a\mu}$, and A^μ, respectively. We use the parameter set TM1 (Sugahara & Toki 1994) as give in Table 1. It is known that the RMF theory with the parameter set TM1 can reproduce good saturation properties of nuclear matter and satisfactory description of finite nuclei (Sugahara & Toki 1994; Hirata et al. 1996).

Starting with the Lagrangian (1), we derive a set of Euler–Lagrange equations. In the RMF approximation, the meson fields are considered as classical fields and they are replaced by their expectation values. For a static system, the non-vanishing expectation values are $\sigma = \langle\sigma\rangle$, $\omega = \langle\omega^0\rangle$, $\rho = \langle\rho^{30}\rangle$, and $A = \langle A^0\rangle$. The equations of motion for these mean fields have the following form:

$$-\nabla^2\sigma + m_\sigma^2\sigma + g_2\sigma^2 + g_3\sigma^3 = -g_\sigma n_s, \tag{2}$$

$$-\nabla^2\omega + m_\omega^2\omega + c_3\omega^3 = g_\omega n_v, \tag{3}$$

$$-\nabla^2\rho + m_\rho^2\rho = g_\rho n_3, \tag{4}$$

$$-\nabla^2 A = e n_c, \tag{5}$$

where n_s, n_v, n_3, and n_c are the scalar, vector, third component of isovector, and charge densities, respectively. The stationary Dirac equation for nucleons is given by

$$\left(-\alpha\cdot\nabla + \beta M^* + g_\omega\omega + g_\rho\tau_3\rho + e\frac{1+\tau_3}{2}A\right)\psi^i = \varepsilon^i\psi^i, \tag{6}$$

where $M^* = M + g_\sigma\sigma$ is the effective nucleon mass. i denotes the index of eigenstates, while ε^i is the single-particle energy.

For non-uniform matter at subnuclear densities, heavy nuclei exist in order to decrease the free energy. We assume that each spherical nucleus is located in the center of a charge-neutral cell consisting of a vapor of nucleons and electrons. In the present study, we focus on estimating the difference between the STF and PTF approximations, so we ignore the contribution of alpha-particles for simplicity. The alpha-particle fraction has been shown in Figure 6 of Shen et al. (2011), and moreover the contributions from alpha-particles and other light nuclei have been extensively discussed in Sumiyoshi et al. (2008) and Hempel & Schaffner-Bielich (2010). We assume that nuclei are arranged in a body-centered-cubic (BCC) lattice to minimize the Coulomb lattice energy (Oyamatsu 1993). The Wigner–Seitz cell is introduced to simplify the energy of a unit cell, which is a sphere with the same volume as the unit cell in the BCC lattice. The lattice constant a and the radius of the Wigner–Seitz cell R_C are related to the cell volume by $V_{\rm cell} = a^3 = 4\pi R_C^3/3 = N_B/n_B$, where N_B and n_B are the baryon number per cell and the average baryon number density, respectively.

In the STF approximation, the nucleon distribution function at position r inside the Wigner–Seitz cell is obtained by

$$n_i(r) = \frac{1}{\pi^2}\int_0^\infty dk\, k^2\, \left[f_i^k(r) - f_{\bar{i}}^k(r)\right], \tag{7}$$

where f_i^k and $f_{\bar{i}}^k$ ($i = p,\, n$) are the occupation probabilities of the particle and antiparticle for momentum k. At zero temperature, $f_i^k = 1$ under the Fermi surface and $f_i^k = 0$ above

the Fermi surface. At finite temperature, the occupation probability is obtained by the Fermi–Dirac distribution,

$$f_i^k = \frac{1}{1+\exp\left[\left(\sqrt{k^2+M^{*2}}-\nu_i\right)/T\right]}, \tag{8}$$

$$f_{\bar{i}}^k = \frac{1}{1+\exp\left[\left(\sqrt{k^2+M^{*2}}+\nu_i\right)/T\right]}. \tag{9}$$

The chemical potential μ_i is related to the effective chemical potential ν_i as

$$\mu_p = \nu_p + g_\omega\omega + g_\rho\rho + eA, \tag{10}$$

$$\mu_n = \nu_n + g_\omega\omega - g_\rho\rho. \tag{11}$$

We note that the chemical potential is spatially constant throughout the Wigner–Seitz cell, while other quantities such as occupation probabilities and mean-field values depend on the position r. As for the electrons, we disregard the electron screening effect caused by the non-uniform charged particle distributions, and assume the electron density is uniform. It was found in Maruyama et al. (2005) that the electron screening effect is very small at subnuclear densities. For given average baryon density n_B and proton fraction Y_p, the electrons do not play any role in the free energy minimization, therefore, we ignore the electron contribution as done in Shen et al. (2011).

The free energy per cell contributed from baryons is given by

$$F_{\rm cell} = E_{\rm cell} - TS_{\rm cell}, \tag{12}$$

where $E_{\rm cell}$ and $S_{\rm cell}$ denote the energy and entropy per cell, respectively. The energy per cell can be written as

$$E_{\rm cell} = \int_{\rm cell} \epsilon(r) d^3r + \Delta E_C, \tag{13}$$

with ΔE_C being the correction term for the BCC lattice (Oyamatsu 1993; Shen et al. 2011). This correction is negligible when the nuclear size is much smaller than the cell size. The entropy per cell is given by

$$S_{\rm cell} = \int_{\rm cell} s(r) d^3r. \tag{14}$$

Here $\epsilon(r)$ and $s(r)$ are the local energy density and entropy density at the radius r, which can be calculated by using the RMF theory and the STF approximation. The energy density

in the STF approximation is given by

$$\begin{aligned}\epsilon &= \sum_{i=p,n} \frac{1}{\pi^2} \int_0^\infty dk\, k^2 \sqrt{k^2 + M^{*2}} \left(f_i^k + f_{\bar{i}}^k\right) \\ &+\frac{1}{2}(\nabla\sigma)^2 + \frac{1}{2}m_\sigma^2\sigma^2 + \frac{1}{3}g_2\sigma^3 + \frac{1}{4}g_3\sigma^4 \\ &-\frac{1}{2}(\nabla\omega)^2 - \frac{1}{2}m_\omega^2\omega^2 - \frac{1}{4}c_3\omega^4 + g_\omega\omega\left(n_p + n_n\right) \\ &-\frac{1}{2}(\nabla\rho)^2 - \frac{1}{2}m_\rho^2\rho^2 + g_\rho\rho\left(n_p - n_n\right) \\ &-\frac{1}{2}(\nabla A)^2 + eA\left(n_p - n_e\right), \end{aligned} \tag{15}$$

the entropy density is given by

$$\begin{aligned} s &= \sum_{i=p,n} \frac{1}{\pi^2} \int_0^\infty dk\, k^2 \quad \left[-f_i^k \ln f_i^k - \left(1 - f_i^k\right) \ln\left(1 - f_i^k\right)\right. \\ &\qquad \left. -f_{\bar{i}}^k \ln f_{\bar{i}}^k - \left(1 - f_{\bar{i}}^k\right) \ln\left(1 - f_{\bar{i}}^k\right)\right]. \end{aligned} \tag{16}$$

Here, we have omitted the electron kinetic energy and electron entropy, which do not play any role in the free energy minimization. It is known that nuclear pasta phases could present at subnuclear densities before the transition to uniform matter. In this study, we consider both droplet and bubble phases. The free energy for bubble phase can also be calculated from Equation (12), but with different correction term ΔE_C (Oyamatsu 1993).

It is interesting and important to compare the difference between the STF used in this study and the PTF adopted in Shen et al. (2011). In the PTF approximation, the energy per cell is given in the form

$$E_{\rm cell}^{\rm PTF} = E_{\rm cell}^b + E_{\rm cell}^g + E_{\rm cell}^C, \tag{17}$$

where $E_{\rm cell}^b$ is the bulk energy per cell given by Equation (20) of Shen et al. (2011). The surface (gradient) energy term $E_{\rm cell}^g$ due to the inhomogeneity of the nucleon distribution is assumed to have the form

$$E_{\rm cell}^g = \int_{\rm cell} F_0 \mid \nabla\left[\, n_n\left(r\right) + n_p\left(r\right)\right] \mid^2 d^3r, \tag{18}$$

with the parameter $F_0 = 70\,{\rm MeV\,fm^5}$ determined by the gross properties of nuclear masses and charge radii (Oyamatsu 1993; Shen et al. 2011). The Coulomb energy term $E_{\rm cell}^C$ can be calculated as

$$E_{\rm cell}^C = \frac{1}{2}\int_{\rm cell} eA\left(r\right)\left[n_p\left(r\right) - n_e\right] d^3r + \Delta E_C, \tag{19}$$

where $A(r)$ is the electrostatic potential and ΔE_C is the same as that of Equation (13). By comparing Equation (17) with Equation (13), we recognize that the Coulomb energy in STF and PTF can be calculated in the same way as given by Equation (19), but the surface (gradient) energy is treated differently. In the STF approximation the gradient energy is included in Equation (15) self-consistently, while it is calculated by Equation (18) with an additional parameter F_0 in the PTF approximation. This may cause some differences in energy between these two methods. Another difference between STF and PTF is that the nucleon distribution function $n_i(r)$ ($i = p$ or n) is determined self-consistently in the STF approximation by solving Equations (2)-(5) inside the Wigner–Seitz cell. In the PTF method, the nucleon distribution function is assumed to have the form (Oyamatsu 1993; Shen et al. 2011)

$$n_i(r) = \begin{cases} \left(n_i^{\rm in} - n_i^{\rm out}\right)\left[1 - \left(\frac{r}{R_i}\right)^{t_i}\right]^3 + n_i^{\rm out}, & 0 \le r \le R_i, \\ n_i^{\rm out}, & R_i \le r \le R_C. \end{cases} \tag{20}$$

It is important to examine the effect of these differences on thermodynamic quantities at subnuclear densities, so that we can estimate how good/bad the PTF approximation is in Shen et al. (2011).

We minimize the free energy per baryon, $F = F_{\rm cell}/N_B$, at given temperature T, proton fraction Y_p, and baryon mass density ρ_B. Note that the baryon mass density is defined as $\rho_B = m_u n_B$ with m_u being the atomic mass unit (Shen et al. 2011). The thermodynamically favored state is the one with the lowest F among all configurations considered. In the PTF approximation, the minimization procedure was realized with respect to several independent parameters as described in Shen et al. (2011). In the STF approximation, we minimize F with respect to the Wigner–Seitz cell radius, R_C, and finally determine the most stable configuration among droplet, bubble, and homogeneous phases by comparing their free energies. To compute $F_{\rm cell}$ at a fixed R_C, we numerically solve the coupled Equations (2)-(5) together with the nucleon distribution and occupation probability given by Equations (7)-(9) in coordinate space. Starting from an initial guess for the mean-field values $\sigma(r)$, $\omega(r)$, $\rho(r)$, and $A(r)$, we determine the chemical potential μ_i ($i = p$ or n) by the condition $\int_0^{R_C} n_i(r) 4\pi r^2 dr = N_i$, where the proton and neutron numbers per cell are respectively given by $N_p = Y_p N_B$ and $N_n = (1 - Y_p) N_B$. Once the chemical potentials are known, the occupation probabilities and density distributions can be obtained. Then, using these densities we solve Equations (2)-(5) to get new mean-field values. This procedure is iterated until self-consistency is achieved. For the numerical integrations in coordinate space, we use a composite Simpson's rule with 1201 grid points. In general, this number of grid points is sufficient to achieve good convergence in both solving coupled equations and performing numerical integrations.

3. Results and discussion

In this section, we show and discuss the results of the non-uniform matter at subnuclear densities obtained using the STF approximation. In comparison with the PTF method used in Shen et al. (2011), the nucleon distribution and the surface effect are self-consistently calculated within the STF approximation. In addition, we take into account the bubble phase that may be present before the transition to uniform matter.

At given temperature T, proton fraction Y_p, and baryon mass density ρ_B, we minimize the free energy per baryon, $F = F_{\rm cell}/N_B$, with respect to the independent variables in the model. In the STF approximation, there is only one independent variable, namely the cell radius R_C. However, there are about seven independent variables ($n_n^{\rm in}$, R_n, t_n, $n_p^{\rm in}$, R_p, t_p, and R_C) in the PTF approximation (Shen et al. 2011). It is interesting and important to make a detailed comparison between STF and PTF. In Figure 1, we show the resulting free energy per baryon F versus the baryon mass density ρ_B for $Y_p = 0.3$ and 0.5 at $T = 1$ MeV and 10 MeV. Note that we focus here on the non-uniform matter phase in which heavy nuclei are formed in the medium-density and low-temperature region, while the behavior of F and other thermodynamic quantities over the wide range of EOS has been discussed in our earlier work (Shen et al. 1998b, 2011). We present in Figure 1 the results of STF (PTF) with a droplet configuration by black solid (blue dashed) lines. The bubble phase is also taken into account in the STF calculation as shown by red dash-dotted lines. It is shown that the onset density of the bubble phase is above $10^{13.9}\,{\rm g\,cm^{-3}}$. The inclusion of the bubble phase causes a visible decrease in the free energy at $\rho_B > 10^{13.9}\,{\rm g\,cm^{-3}}$. On the other hand, the appearance of the bubble phase can delay the transition to uniform matter as indicated by the vertical dashed lines. We find that there is a small difference in F between STF and PTF, especially in the case of $T = 1$ MeV (top panel). The free energy per baryon F obtained in PTF is systematically lower than that of STF for the same droplet configuration. This may be due to the different treatment of surface effect and nucleon distribution between these two methods. In order to estimate how much difference can be caused by the different treatment of surface effect, we should compare corresponding terms in Equation (17). However, it is difficult in the STF approximation to separate the gradient energy from the bulk energy, because both of them are involved in the first term of Equation (13). On the other hand, the Coulomb energy can be easily separated from Equation (13) as defined by Equation (19), so that it is possible to compare the difference in the Coulomb energy between STF and PTF. In Oyamatsu (1993) and Oyamatsu & Iida (2003), the authors have pointed out that the gradient energy in equilibrium should be as large as the Coulomb energy in general cases, which means that $E_{\rm cell}^g \simeq E_{\rm cell}^C$ could hold in both STF and PTF. This relation corresponds to the well-known equilibrium condition in the liquid-drop model that the surface energy is twice as much as the Coulomb energy. In the results of PTF, we do obtain $E_{\rm cell}^g = E_{\rm cell}^C$ (see

Table 2). Therefore, we can use the relation $E^g_{\rm cell} = E^C_{\rm cell}$ to estimate the gradient energy in the STF approximation, and define the bulk energy as $E^b_{\rm cell} = E_{\rm cell} - E^g_{\rm cell} - E^C_{\rm cell}$. In Table 2, we compare various quantities between STF and PTF for the cases of $Y_p = 0.3$ and $T = 1$ MeV. The definitions of these quantities are as follows: $F = F_{\rm cell}/N_B$ is the free energy per baryon, $E = E_{\rm cell}/N_B$ is the energy per baryon, $S = S_{\rm cell}/N_B$ is the entropy per baryon, $E_b = E^b_{\rm cell}/N_B$ is the bulk energy per baryon, $E_g = E^g_{\rm cell}/N_B$ is the gradient energy per baryon, $E_C = E^C_{\rm cell}/N_B$ is the Coulomb energy per baryon, and R_C is the radius of the Wigner–Seitz cell. Note that $F_0 = 70\,{\rm MeV\,fm^5}$ has been used in the PTF method (Shen et al. 2011), so we first compare the results of STF with those of PTF ($F_0 = 70$). It is shown that there is no much difference in S and E_b, but F, E, E_g, and E_C of PTF ($F_0 = 70$) are all slightly lower than those of STF. Furthermore, the difference in F (which is 0.217 MeV at $\rho_B = 10^{13.0}\,{\rm g\,cm^{-3}}$) is about twice as much as that in E_C (~ 0.1 MeV). This implies that the difference in F is mostly caused by the sum $E_g + E_C = 2E_g$, namely the surface effect. It seems that E_g with $F_0 = 70\,{\rm MeV\,fm^5}$ in the PTF approximation is relatively small compared to the self-consistent calculation of STF. To analyze the influence of the parameter F_0, we recalculated the results of PTF with $F_0 = 90\,{\rm MeV\,fm^5}$, that are also listed in Table 2. By comparing the results of PTF ($F_0 = 70$) and PTF ($F_0 = 90$), we find that E_g and E_C of PTF ($F_0 = 90$) are significantly enhanced and closer to the values of STF. As a results, the differences in F between STF and PTF ($F_0 = 90$) are much smaller than those between STF and PTF ($F_0 = 70$). Since E_g and E_C of PTF ($F_0 = 90$) are very close to the values of STF, the small differences in F between STF and PTF ($F_0 = 90$) should be caused by the different treatment of nucleon distributions between these two methods. In the last column of Table 2, we compare the cell radius R_C obtained by different methods. It is shown that R_C of PTF ($F_0 = 70$) is obviously smaller than that of STF and PTF ($F_0 = 90$). This is because a smaller surface energy favors a smaller nuclear size and cell radius based on the liquid-drop model (Maruyama et al. 2005). Therefore, the increase of the surface energy in PTF ($F_0 = 90$) leads to a larger R_C compared to that in PTF ($F_0 = 70$). In the bottom panel of Figure 1, we show the results for the case of $T = 10$ MeV. The density range of the non-uniform matter phase at high temperature becomes very narrow as shown in Figure 2 of Shen et al. (2011), so we just compare the results in this density range. It is seen that the differences between STF and PTF at $T = 10$ MeV (bottom panel) are generally smaller than those at $T = 1$ MeV (top panel). This is because at higher temperature the entropy becomes more dominant and the treatment of surface effect plays a less important role in determining the free energy.

We plot in Figure 2 the entropy per baryon S versus ρ_B for $Y_p = 0.3$ and 0.5 at $T = 1$ MeV and 10 MeV. In the case of $T = 1$ MeV (top panel), there is almost no difference between STF and PTF for $Y_p = 0.3$ (also see Table 2), while there is a small difference in

the case of $Y_p = 0.5$. At $T = 10$ MeV (bottom panel), the results of STF and PTF are almost identical for both $Y_p = 0.3$ and $Y_p = 0.5$. We note that the behavior of the entropy has a strong Y_p dependence, which is due to the formation of heavy nuclei as discussed in Shen et al. (1998b, 2011).

In Figures 3 and 4, we show the density distributions of protons and neutrons inside the Wigner–Seitz cell for the cases of $Y_p = 0.3$ at $T = 1$ MeV and $T = 10$ MeV, respectively. The horizontal axis denotes the radial distance from the center of the cell, while the cell radius is indicated by the hatch. The results obtained in STF (black solid lines) are compared with those of PTF (blue dashed lines). At lower densities, there is no obvious difference in the density profiles between STF and PTF. However, as density increases, the difference becomes noticeable as shown in the top panels. It is seen that the densities at the center of the cell are significantly lower than those at the surface region obtained in the STF approximation. This is because the Coulomb interaction is explicitly included in the equation of motion for the protons, and as a result, more protons are pushed off to the surface. The same behavior has been observed in Maruyama et al. (2005) where the authors compare results obtained with different treatment of the Coulomb interaction. In the STF approximation, the nucleon distributions are obtained self-consistently with the cell radius R_C determined by the free energy minimization. However, the nucleon distributions in the PTF approximation are forced to have the form of Equation (20) with all parameters including R_C determined in the minimization procedure. Comparing the results of $T = 10$ MeV (Figure 4) with those of $T = 1$ MeV (Figure 3), the differences between STF and PTF are very similar. It is shown that more free nucleons exist outside the nuclei in the case of $T = 10$ MeV. This is because at higher temperature the entropy becomes more dominant, and as a result, the free energy could be decreased by more nucleons dripping out of the nuclei. In both Figures 3 and 4, the cell radius R_C obtained in STF is obviously larger than that of PTF. This is related to the treatment of surface effect as discussed above. It is known based on the liquid-drop model that a smaller surface energy favors a smaller nuclear size and cell radius (Maruyama et al. 2005). In the PTF method, $F_0 = 70\,\mathrm{MeV\,fm^5}$ has been used in the calculation of surface (gradient) energy, which seems not large enough in comparison with the results of STF (see Table 2). Therefore, the smaller surface energy of PTF leads to a smaller R_C compared to that of STF.

We consider both droplet and bubble phases in this study. It is found that the bubble could have a lower free energy than the droplet near the transition density to uniform matter. In Figure 5, we show the density distributions of protons and neutrons obtained with droplet and bubble configurations using the STF approximation for the cases of $Y_p = 0.3$ and $\rho_B = 10^{14.0}\,\mathrm{g\,cm^{-3}}$ at $T = 1$ MeV (top panel) and $T = 10$ MeV (bottom panel). We minimize the free energy per baryon with respect to the cell radius for both droplet and bubble

configurations, and then determine the most stable droplet and bubble. By comparing their free energies, we determine which is the most favorable configuration among droplet, bubble, and homogeneous phases. The onset of the bubble phase can be seen in Figure 1. Generally, the bubble has the lowest free energy at $\rho_B \sim 10^{14}\,\mathrm{g\,cm^{-3}}$ ($n_B \sim 0.06\,\mathrm{fm^{-3}}$). We present in Table 3 the resulting properties of stable droplet and bubble in the STF approximation, while the results of PTF and those of uniform matter are also listed for comparison. It is shown that the difference in F between the droplet and bubble phases is less than 1%, but there are significant differences in μ_p and μ_n. On the other hand, the inclusion of the bubble phase can increase the transition density to uniform matter. For instance, at $\rho_B = 10^{14.2}\,\mathrm{g\,cm^{-3}}$ with $Y_p = 0.3$ and $T = 1$ MeV, the bubble phase has the lowest free energy among droplet, bubble, and homogeneous phases, but it favors the homogeneous phase if the bubble configuration is not taken into account.

We examine the droplet properties in non-uniform matter and investigate their density dependence. In Figure 6, we show the nuclear mass number A_d and charge number Z_d inside the droplet as a function of ρ_B for the cases of $Y_p = 0.3$ at $T = 1$ MeV (top panel) and $T = 10$ MeV (bottom panel). Note that these quantities are different from those shown in Figure 5 of Shen et al. (2011). Here the background nucleon gas is subtracted in order to isolate the nucleus from the surrounding nucleon gas, namely $A_d = N_B - V_{\rm cell} n_B(R_C)$ and $Z_d = N_p - V_{\rm cell} n_p(R_C)$. This subtraction procedure has been widely used in Thomas–Fermi calculations (De et al. 2001; Gril et al. 2012). For comparison, we calculate A_d and Z_d using the PTF approximation and show with blue dashed lines. It is seen that A_d and Z_d increase rapidly with increasing density. At the same ρ_B and Y_p, the values of A_d and Z_d at $T = 10$ MeV are significantly less than those at $T = 1$ MeV, which is due to more nucleons can drip out of the nuclei at higher temperature. It is found that there is a small difference between STF and PTF for both $T = 1$ MeV and $T = 10$ MeV. This should be related to the difference in nucleon distributions as shown in Figures 3 and 4. Generally, the droplet properties obtained in STF are very similar to those of PTF. In Figure 7, we show the fractions of nuclei (X_A), neutron gas (X_n), and proton gas (X_p) as a function of ρ_B for the same case as Figure 6. These fractions are defined by $X_A = A_d/N_B$, $X_n = V_{\rm cell} n_n(R_C)/N_B$, and $X_p = V_{\rm cell} n_p(R_C)/N_B$. In the case of $T = 1$ MeV and $Y_p = 0.3$ (top panel), there is almost no proton gas ($X_p \simeq 0$), while the neutron gas fraction X_n is very small and decreases with increasing density. This implies that nucleons inside the droplet are dominant at low temperature. For the case of $T = 10$ MeV and $Y_p = 0.3$ (bottom panel), more nucleons can drip out of the nuclei as shown in Figures 4, and as a result X_n is of the same order of X_A, while X_p is about one order lower than X_n. Comparing the results between STF and PTF, it is hard to see any significant difference at $T = 10$ MeV (bottom panel), while there is a small difference in X_n at $T = 1$ MeV (top panel).

In Figures 8 and 9, we show the chemical potentials of protons and neutrons, μ_p and μ_n, as a function of ρ_B with $Y_p = 0.3$ and 0.5 at $T = 1$ MeV and 10 MeV. The results of PTF are taken from EOS2 of Shen et al. (2011), which were calculated through the thermodynamic relations given in Equations (A16) and (A17) of Shen et al. (2011). In the STF approximation, the chemical potentials given in Equations (10) and (11) are obtained self-consistently as described in Section 2, which are spatially constant throughout the Wigner–Seitz cell. It is shown that the appearance of the bubble phase at $\rho_B > 10^{13.9}\,\mathrm{g\,cm^{-3}}$ causes sudden jumps in μ_p and μ_n within the STF approximation. This is mainly because the Coulomb potential in the bubble is very different from that in the droplet. As for comparison between STF and PTF, it is found that there are visible differences between STF and PTF in μ_p as shown in Figure 8, while the chemical potentials of neutrons are almost identical between STF and PTF with the same droplet configuration as shown in Figure 9. The difference in μ_p may be related to the difference in Coulomb interaction between STF and PTF. As discussed above, the Coulomb and surface energies in PTF with $F_0 = 70\,\mathrm{MeV\,fm^5}$ is relatively small compared to those of STF, which means that the Coulomb potential in PTF should be smaller than that in STF. According to Equation (10), a larger Coulomb potential corresponds to a higher μ_p. Therefore, we obtain higher μ_p in STF due to its larger Coulomb potential. On the other hand, μ_n is not directly related to the Coulomb potential, so the difference in μ_n between STF and PTF is very small as shown in Figure 9.

4. Conclusion

In this paper, we have studied the non-uniform matter at subnuclear densities using the STF approximation. For the effective nuclear interaction, we have adopted the RMF theory including nonlinear σ and ω terms with the parameter set TM1 which can reproduce good saturation properties of nuclear matter and satisfactory description of finite nuclei. We have made a detailed comparison between the STF approximation used in this study and the PTF approximation adopted in Shen et al. (2011). In addition, we have included the bubble phase that could be present before the transition to uniform matter. It has been found that the inclusion of the bubble phase can significantly affect the chemical potentials of protons and neutrons, while its effects on free energy and entropy are relatively small. Furthermore, the appearance of the bubble phase can delay the transition to uniform matter.

We have examined the difference between STF and PTF. In the STF method, the nucleon distribution and the surface effect are treated self-consistently. We have minimized the free energy with respect to the cell radius at given temperature T, proton fraction Y_p, and baryon mass density ρ_B. The thermodynamically favored state is the one with the lowest free

energy among all configurations considered. The results obtained in the STF approximation have been compared with those of PTF. It have been found that there is no obvious difference in nucleon distributions at lower densities, while the difference becomes noticeable near the transition density to uniform matter. For thermodynamical quantities, such as the free energy and entropy per baryon, the results of both methods generally agree well with each other. However, there are some small differences between STF and PTF which need to be analyzed. The free energy per baryon obtained in PTF is slightly lower than that of STF for the same droplet configuration. This is mainly caused by the inconsistent treatment of the surface effect in PTF, namely the surface and Coulomb energies with the parameter $F_0 = 70\,\mathrm{MeV\,fm^5}$ is relatively small compared to those obtained self-consistently in STF. In addition, the smaller surface energy in PTF leads to a smaller cell radius in comparison to that of STF. On the other hand, the proton chemical potential obtained in STF is slightly higher than that of PTF, which is also related to the difference in the Coulomb and surface energies between STF and PTF. Therefore, we can draw the conclusion that most of the differences between STF and PTF should be due to the different treatment of surface effect, namely the parameter F_0 used in PTF is not large enough in comparison with the results obtained in the STF approximation.

Considering the wide range of thermodynamic conditions in the whole EOS (Shen et al. 2011), the differences between STF and PTF are thought to be negligible and cannot affect the general behavior of the EOS. Therefore, we conclude that the PTF approximation is a reasonable description for non-uniform matter, and can produce very similar EOS with that obtained in the STF approximation which is considered to be self-consistent in the treatment of surface effect and nucleon distribution.

This research is supported in part by the National Natural Science Foundation of China (Grants No. 11075082 and No. 11375089).

REFERENCES

Avancini, S. S., Brito, L., Marinelli, J. R., Menezes, D. P., Moraes, M. M. W., Providência, C., & Santos, A. M. 2009, Phys. Rev. C, 79, 035804

Avancini, S. S., Chiacchiera, S., Menezes, D. P., & Providência, C. 2010, Phys. Rev. C, 82, 055807

Blinnikov, S. I., Panov, I. V., Rudzsky, M. A., & Sumiyoshi, K. 2011, A&A, 535, A37

Burrows, A., & Lattimer, J. M. 1984, ApJ, 285, 294

Burrows, A., Livne, E., Dessart, L., Ott, C. D., & Murphy, J. 2006, ApJ, 640, 878

Centelles, M., Schuck, P., & Viñas, X. 2007, Ann. Phys., 322, 363

De, J. N., Viñas, X., Patra, S. K., & Centelles, M. 2001, Phys. Rev. C, 64, 057306

Furusawa, S., Yamada, S., Sumiyoshi, K., & Suzuki, H. 2011, ApJ, 738, 178

Furusawa, S., Sumiyoshi, K., Yamada, S., & Suzuki, H. 2013, ApJ, 772, 95

Grill, F., Providência, C., & Avancini, S. S. 2012, Phys. Rev. C, 85, 055808

Hempel, M., & Schaffner-Bielich, J. 2010, Nucl. Phys. A, 837, 210

Hirata, D., Sumiyoshi, K., Carlson, B. V., Toki, H., & Tanihata, I. 1996, Nucl. Phys. A, 609, 131

Janka, H.-Th., Langanke, K., Marek, A., Martínez-Pinedo, G., & Müller, B. 2007, Phys. Rep., 442, 38

Lattimer, J. M., & Swesty, F. D. 1991, Nucl. Phys. A, 535, 331

Lattimer, J. M., & Prakash, M. 2007, Phys. Rep., 442, 109

Maruyama, T., Tatsumi, T., Voskresensky, D. N., Tanigawa, T., & Chiba, S. 2005, Phys. Rev. C, 72, 015802

Oyamatsu, K. 1993, Nucl. Phys. A, 561, 431

Oyamatsu, K., & Iida, K. 2003, Prog. Theor. Phys., 109, 631

Schaffner, J., & Mishustin, I. N. 1996, Phys. Rev. C, 53, 1416

Serot, B. D., & Walecka, J. D. 1986, Adv. Nucl. Phys., 16, 1

Shen, G., Horowitz, C. J., & Teige, S. 2010, Phys. Rev. C, 82, 015806

Shen, H., Toki, H., Oyamatsu, K., & Sumiyoshi, K. 1998a, Nucl. Phys. A, 637, 435

Shen, H., Toki, H., Oyamatsu, K., & Sumiyoshi, K. 1998b, Prog. Theor. Phys., 100, 1013

Shen, H., Toki, H., Oyamatsu, K., & Sumiyoshi, K. 2011, Astrophys. J. Suppl., 197, 20

Sugahara, Y., & Toki, H. 1994, Nucl. Phys. A, 579, 557

Sumiyoshi, K., Yamada, S., Suzuki, H., Shen, H., Chiba, S., & Toki, H. 2005, ApJ, 629, 922

Sumiyoshi, K., & Röpke, G. 2008, Phys. Rev. C, 77, 055804

Sumiyoshi, K., Ishizuka, C., Ohnishi, A., Yamada, S., & Suzuki, H. 2009, ApJ, 690, L43

Weber, F. 2005, Prog. Part. Nucl. Phys., 54, 193

This preprint was prepared with the AAS LaTeX macros v5.2.

Table 1. Parameter set TM1 for the RMF Lagrangian used in this work. The masses are given in MeV.

M	m_σ	m_ω	m_ρ	g_σ	g_ω	g_ρ	g_2 (fm^{-1})	g_3	c_3
938.0	511.19777	783.0	770.0	10.02892	12.61394	4.63219	-7.23247	0.61833	71.30747

Table 2. Comparison between different methods for the cases of $Y_p = 0.3$ and $T = 1$ MeV at $\rho_B = 10^{13.0}$, $10^{13.5}$, and $10^{13.9}\,\mathrm{g\,cm^{-3}}$. The various quantities are defined as follows: $F = F_{\mathrm{cell}}/N_B$ is the free energy per baryon, $E = E_{\mathrm{cell}}/N_B$ is the energy per baryon, $S = S_{\mathrm{cell}}/N_B$ is the entropy per baryon, $E_b = E^b_{\mathrm{cell}}/N_B$ is the bulk energy per baryon, $E_g = E^g_{\mathrm{cell}}/N_B$ is the gradient energy per baryon, $E_C = E^C_{\mathrm{cell}}/N_B$ is the Coulomb energy per baryon, and R_C is the radius of the Wigner–Seitz cell.

$\log_{10}(\rho_B)$ ($\mathrm{g\,cm^{-3}}$)	method	F (MeV)	E (MeV)	S (k_B)	E_b (MeV)	E_g (MeV)	E_C (MeV)	R_c (fm)
13.0	STF	-8.087	-7.807	0.280	-10.135	1.164	1.164	20.0
	PTF ($F_0 = 70$)	-8.304	-8.025	0.278	-10.161	1.068	1.068	19.3
	PTF ($F_0 = 90$)	-8.023	-7.748	0.275	-10.080	1.166	1.166	20.3
13.5	STF	-8.577	-8.377	0.201	-10.275	0.949	0.949	16.1
	PTF ($F_0 = 70$)	-8.754	-8.554	0.200	-10.286	0.866	0.866	15.5
	PTF ($F_0 = 90$)	-8.527	-8.326	0.200	-10.223	0.948	0.948	16.3
13.9	STF	-9.275	-9.112	0.163	-10.433	0.660	0.660	16.6
	PTF ($F_0 = 70$)	-9.388	-9.226	0.162	-10.438	0.606	0.606	15.5
	PTF ($F_0 = 90$)	-9.229	-9.066	0.164	-10.386	0.660	0.660	16.4

Table 3. Comparison between different phases for the cases of $Y_p = 0.3$ and $\rho_B = 10^{14.0}\,\mathrm{g\,cm^{-3}}$ at $T = 1$ MeV and 10 MeV. The various quantities are as follows: F is the free energy per baryon, S is the entropy per baryon, μ_n and μ_p are the chemical potentials of neutrons and protons, R_C is the radius of the Wigner–Seitz cell, $n_n(r)$ and $n_p(r)$ are the number densities of neutrons and protons at position r in the cell.

T (MeV)	phase	F (MeV)	S (k_B)	μ_n (MeV)	μ_p (MeV)	R_c (fm)	$n_n(0)$ ($\mathrm{fm^{-3}}$)	$n_p(0)$ ($\mathrm{fm^{-3}}$)	$n_n(R_C)$ ($\mathrm{fm^{-3}}$)	$n_p(R_C)$ ($\mathrm{fm^{-3}}$)
1	Bubble (STF)	-9.615	0.152	-0.678	-40.265	17.13	0.0002	0.0000	0.0780	0.0392
	Droplet (STF)	-9.528	0.155	-0.026	-31.934	18.28	0.0696	0.0263	0.0008	0.0000
	Droplet (PTF)	-9.612	0.155	0.383	-35.873	16.65	0.0807	0.0393	0.0013	0.0000
	Uniform matter	-7.994	0.214	-6.544	-32.140		0.0422	0.0181	0.0422	0.0181
10	Bubble (STF)	-17.527	1.641	-7.843	-39.332	13.51	0.0124	0.0021	0.0559	0.0272
	Droplet (STF)	-17.462	1.686	-8.090	-36.202	13.81	0.0547	0.0256	0.0275	0.0081
	Droplet (PTF)	-17.481	1.661	-7.881	-37.735	14.56	0.0594	0.0297	0.0230	0.0061
	Uniform matter	-17.453	1.738	-8.845	-37.355		0.0422	0.0181	0.0422	0.0181

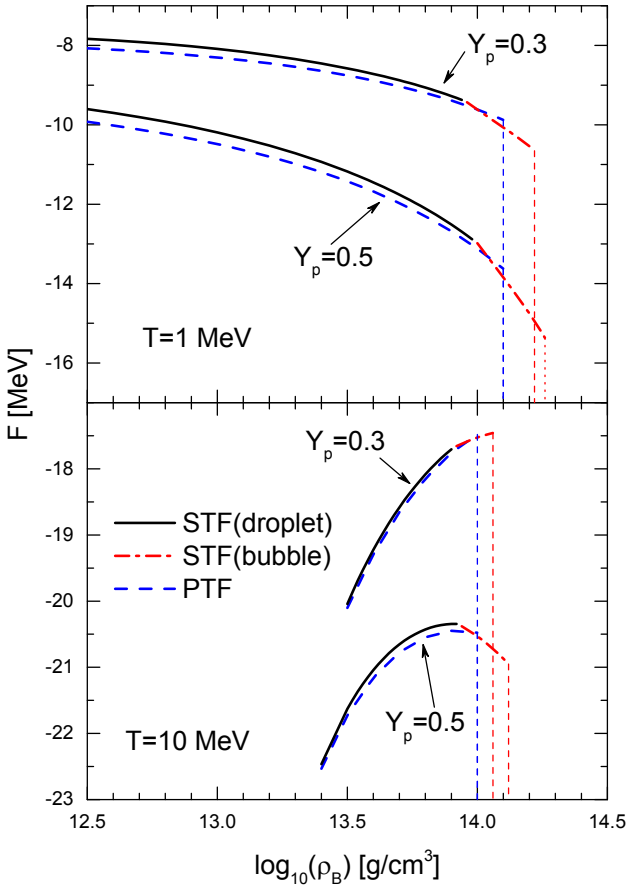

Fig. 1.— Free energy per baryon F versus ρ_B for $Y_p = 0.3$ and 0.5 at $T = 1$ MeV (top panel) and $T = 10$ MeV (bottom panel). The results of STF with droplet configuration (black solid lines) and bubble configuration (red dash-dotted lines) are compared with those of PTF (blue dashed lines). The vertical dashed lines indicate the position where the transition from non-uniform matter to uniform matter occurs. (A color version of this figure is available in the online journal.)

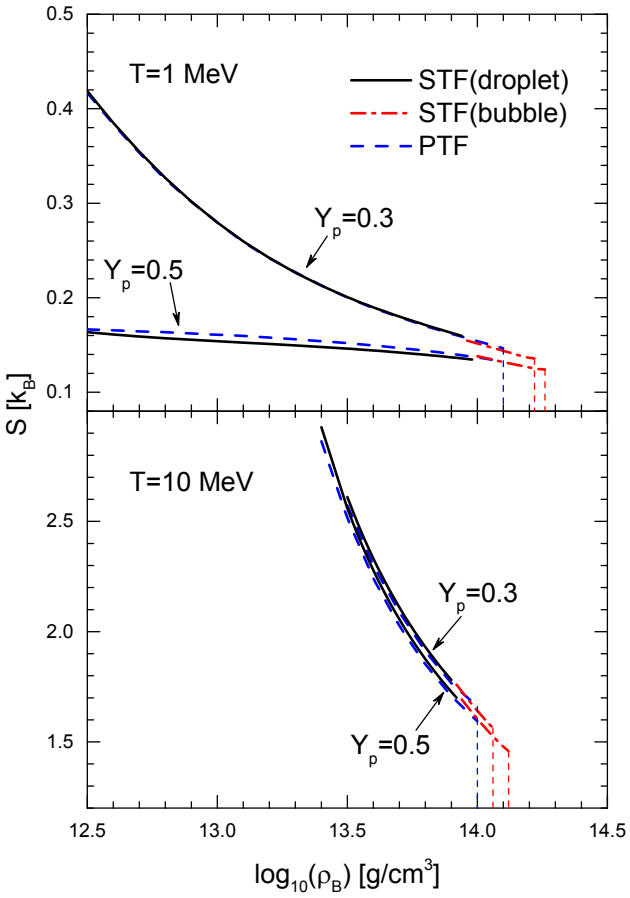

Fig. 2.— Same as Figure 1, but for entropy per baryon S. (A color version of this figure is available in the online journal.)

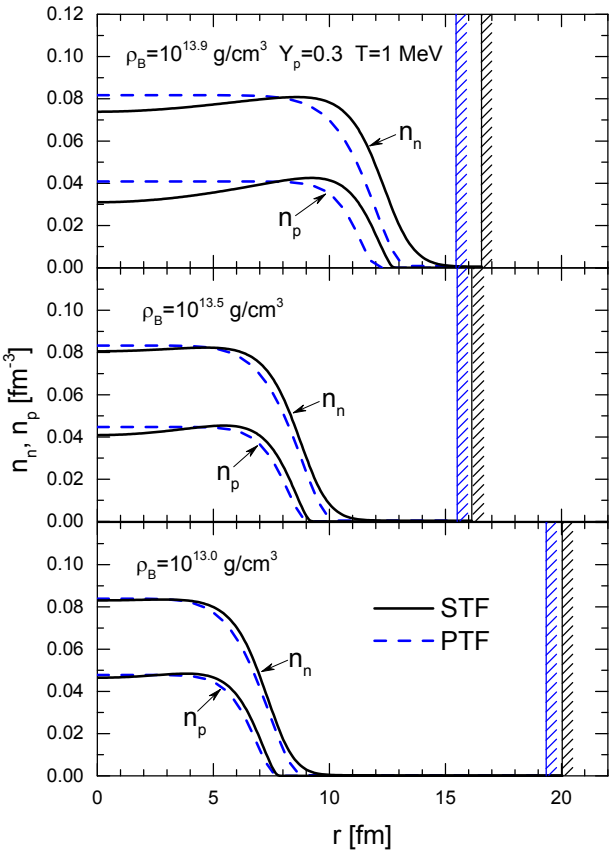

Fig. 3.— Density distributions of protons and neutrons inside the Wigner–Seitz cell for the cases of $Y_p = 0.3$ and $T = 1$ MeV at $\rho_B = 10^{13.0}$, $10^{13.5}$, and $10^{13.9}\,\mathrm{g\,cm^{-3}}$ (bottom to top). The cell radius is indicated by the hatch. The results of STF (black solid lines) are compared with those of PTF (blue dashed lines). (A color version of this figure is available in the online journal.)

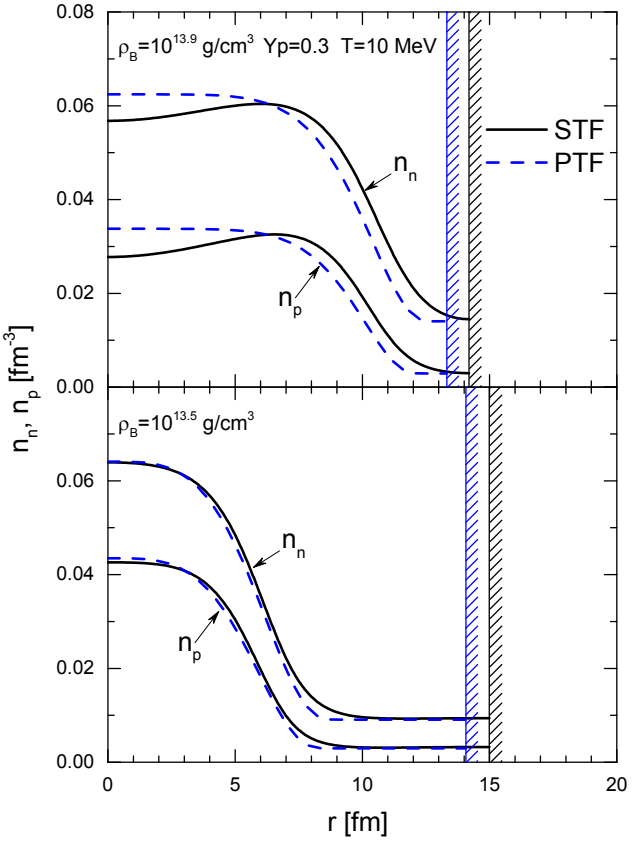

Fig. 4.— Density distributions of protons and neutrons inside the Wigner–Seitz cell for the cases of $Y_p = 0.3$ and $T = 10$ MeV at $\rho_B = 10^{13.5}$ and $10^{13.9}\,\mathrm{g\,cm^{-3}}$ (bottom to top). The cell radius is indicated by the hatch. The results of STF (black solid lines) are compared with those of PTF (blue dashed lines). (A color version of this figure is available in the online journal.)

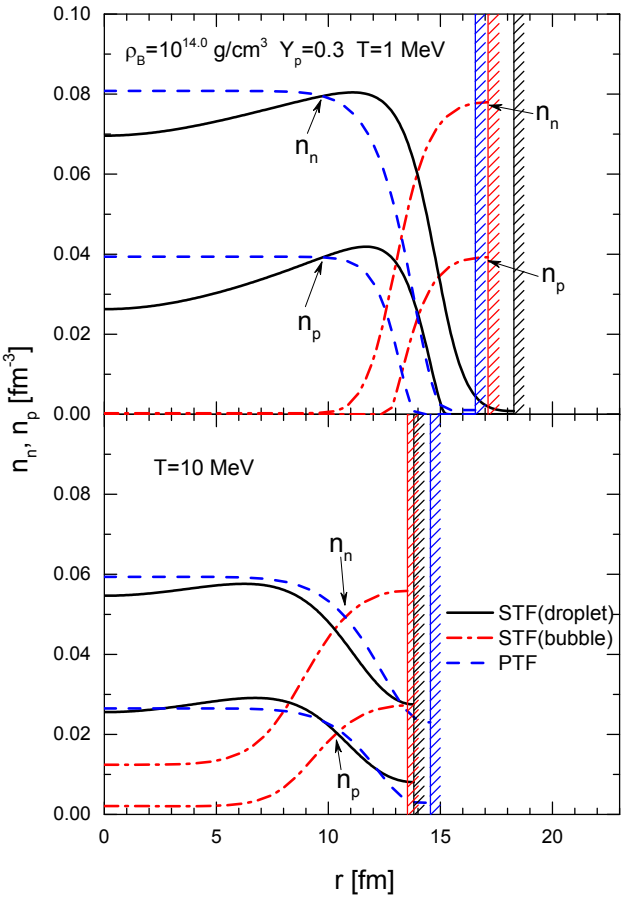

Fig. 5.— Density distributions of protons and neutrons inside the Wigner–Seitz cell for the cases of $Y_p = 0.3$ and $\rho_B = 10^{14.0}\,\mathrm{g\,cm^{-3}}$ at $T = 1$ MeV (top panel) and $T = 10$ MeV (bottom panel). The cell radius is indicated by the hatch. The red dash-dotted lines display the results of STF with bubble configuration. The black solid lines illustrate the results of STF with droplet configuration, while the blue dashed lines show those of PTF for comparison. (A color version of this figure is available in the online journal.)

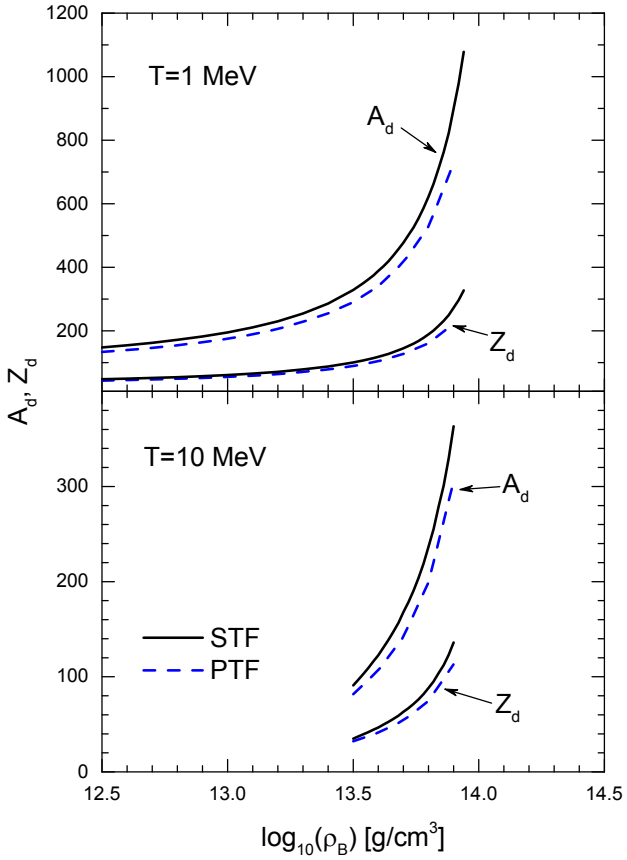

Fig. 6.— Nuclear mass number A_d and charge number Z_d inside the droplet as a function of ρ_B for $Y_p = 0.3$ at $T = 1$ MeV (top panel) and $T = 10$ MeV (bottom panel). Note that A_d and Z_d are defined as excesses with respect to the background nucleon gas using the subtraction procedure. The results of STF (black solid lines) are compared with those of PTF (blue dashed lines). (A color version of this figure is available in the online journal.)

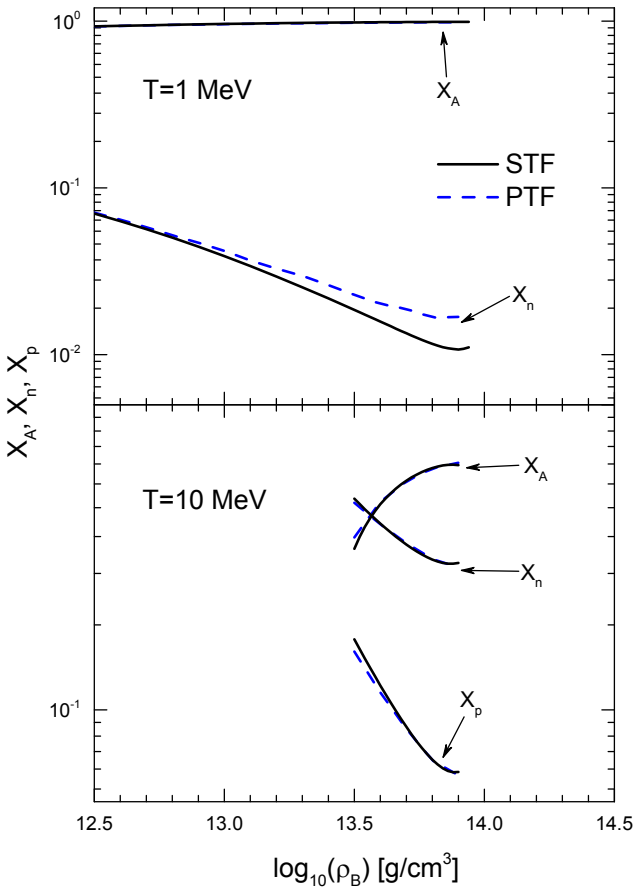

Fig. 7.— Fractions of nuclei (X_A), neutron gas (X_n), and proton gas (X_p) as a function of ρ_B for $Y_p = 0.3$ at $T = 1$ MeV (top panel) and $T = 10$ MeV (bottom panel). Nuclei are defined as excesses with respect to the background nucleon gas using the subtraction procedure. The results of STF (black solid lines) are compared with those of PTF (blue dashed lines). (A color version of this figure is available in the online journal.)

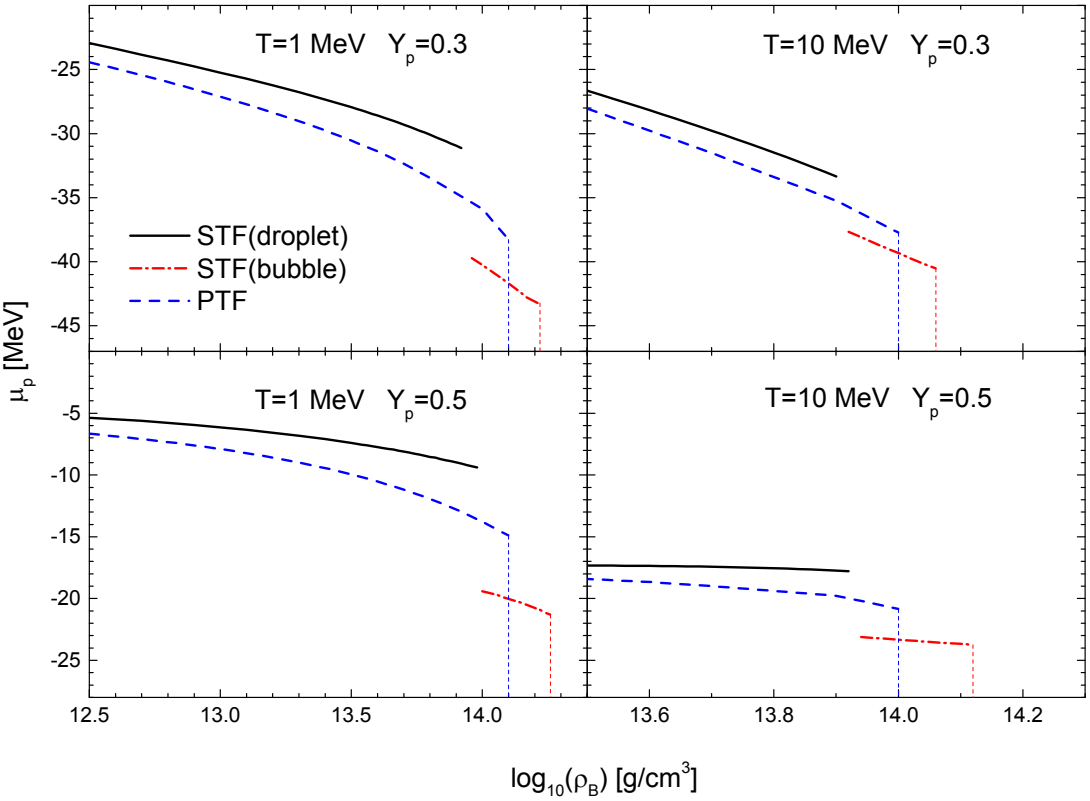

Fig. 8.— Proton chemical potential μ_p as a function of ρ_B for $Y_p = 0.3$ (top panels) and $Y_p = 0.5$ (bottom panels) at $T = 1$ MeV (left panels) and $T = 10$ MeV (right panels). The results of STF with droplet configuration (black solid lines) and bubble configuration (red dash-dotted lines) are compared with those of PTF (blue dashed lines). The onset of the bubble phase at $\rho_B > 10^{13.9}\,\mathrm{g\,cm^{-3}}$ causes sudden jumps in μ_p of STF. The vertical dashed lines indicate the position where the transition from non-uniform matter to uniform matter occurs. (A color version of this figure is available in the online journal.)

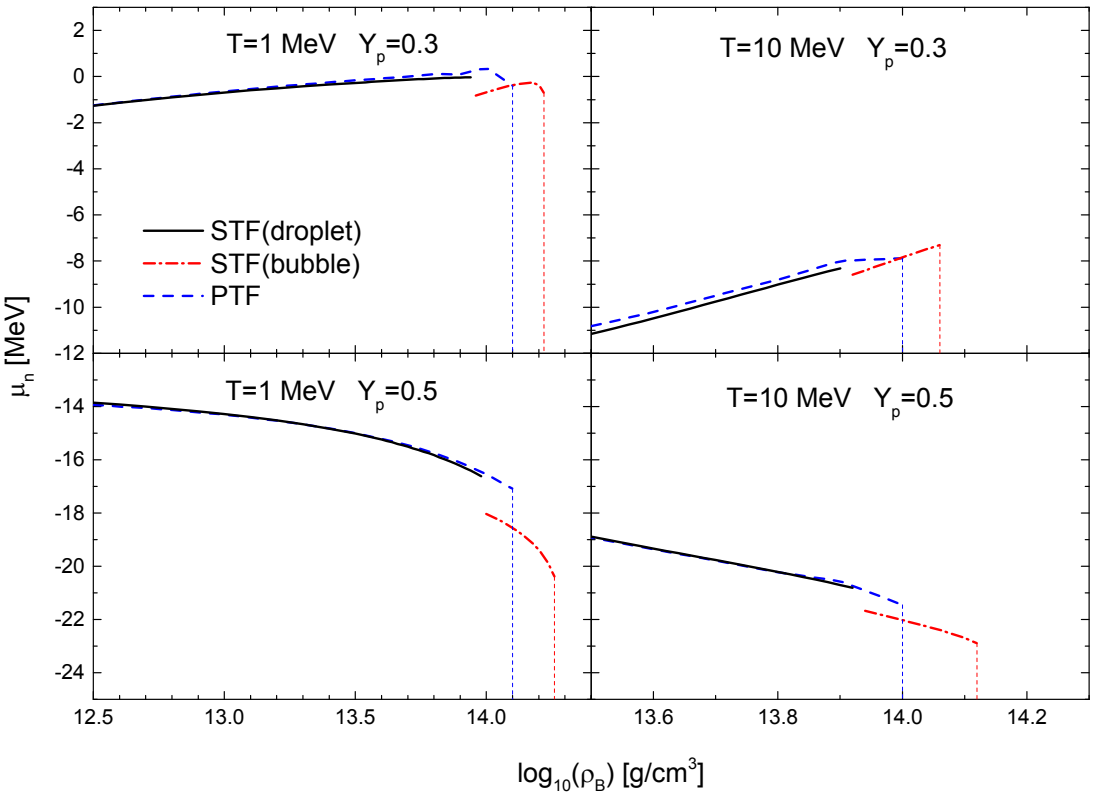

Fig. 9.— Same as Figure 8, but for neutron chemical potential μ_n. (A color version of this figure is available in the online journal.)